

A Phase Field Approach to Model Laser Power Control in Spot Laser Welding

V.Bruyere¹, C. Touvrey^{2*}, P.Namy¹

¹SIMTEC, 8 rue Duployé, Grenoble, 38100 France

²CEA DAM, Valduc, 21120 Is sur Tille

*Corresponding author: CEA DAM, Valduc, 21120 Is sur Tille, charline.touvrey@cea.fr

Abstract: Spot laser welding is largely used in industrial manufacturing, especially in the case of small penetration depth. Unfortunately, welded joints are often polluted by porosities. The formation of porosities depends on complex thermo-hydraulic phenomena.

To understand and control these mechanisms, the COMSOL Multiphysics software is used to model both the interaction and cooling stages of an isolated impact made with a Nd:YAG pulsed laser. The model is based on the Phase Field method in order to apprehend the evolution of the liquid-gas interface shape. The numerical results are compared to experimental characterizations for different operating conditions. At last, the benefic effect of the laser power control (pulse shaping) is demonstrated.

Keywords: Welding, ND:YAG pulsed laser, Thermo-hydraulic, Phase-Field method.

1. Introduction

Spot laser welding is a full-wedged part of industrial manufacturing and is routinely used due to its advantage: it generates very located temperature gradients and therefore, induces small distortions in the pieces. Many welding tests are often performed to minimize the size of the heat affected zone and the number of residual defects. Modeling can thus offer an interesting way to improve the process.

The present study is focused on the physical phenomena modeling during a single pulse of the laser beam. Before vaporization, the laser beam interacts with an almost flat surface, and the rate of absorbed power (absorptivity) is practically constant. When the vaporization point is reached, the ejected vapor induces a pressure called the recoil pressure. It acts as a piston and the liquid-gas interface deforms itself into a deep and narrow cavity called the keyhole. At the end of the interaction, the recoil pressure stops and surface tension forces provoke the collapse of the

keyhole. Gas bubble can then be trapped into the melting pool and give birth to residual porosities according to the solidification time.

Due to the complexity of this multi-physics problem, analytical and semi-analytical approaches are still widely used to study the keyhole dynamics [1]. The aim of this study is to develop a numerical model able to predict the resulting melted zone shape and the porosity formation. To validate our approach, numerical results will thus be confronted to experimental tests on an isolated impact made on a Ti6Al4V sheet [2], especially metallographic data obtained with two different powers and pulse durations. The operating parameters are shown in Table 1.

Table 1: Operating parameters

Parameter	Symbol [Unit]	Value [T_0, T_{fusion}, T_{vap}]
Ambient temperature	T_0 [K]	293.15
Melting point	T_{fusion} [K]	1928
Boiling point	T_{vap} [K]	3600
Melting latent heat	L_f [J.kg ⁻¹]	$3.9 \cdot 10^5$
Evaporation latent heat	L_v [J.kg ⁻¹]	$8.8 \cdot 10^6$
Molar mass	M [kg.mol ⁻¹]	$46.7 \cdot 10^{-3}$
Thermo-density coefficient	β [K ⁻¹]	$1 \cdot 10^{-4}$
Surface tension	γ [N.m ⁻¹]	[-, 1.65, 1.35]
Surface tension variation	$d\gamma / dT$ [N.m ⁻¹ .K ⁻¹]	$-2.7 \cdot 10^{-4}$
Viscosity	η [Pa.s]	$2.2 \cdot 10^{-3}$
Density	ρ [kg.m ⁻³]	[4500, 4200, 3600]
Heat capacity	C_p [J.kg ⁻¹ .K ⁻¹]	[620, 895.2, 895.2]
Conductivity	k [W.m ⁻¹ .K ⁻¹]	[6.2, 30, 42]

After validation, this model can then be used to describe other operating conditions and to improve the process.

2. Modeling

2.1. Laser interaction

The first step consists in modeling the interaction between the laser and the irradiated material. An experimental characterization (illustrated in Figure 1) is used to obtain the laser flux distribution as a function of space (r, z).

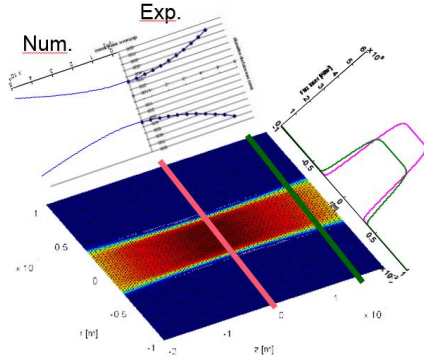


Figure 1. Spatial distribution of the laser beam

As detailed in [2], the resulting spatial repartition of the inward thermal flux is then described by:

$$\text{Flux}_{\text{Laser}} = \text{Abs}_{\text{eq}} \cdot P_{\text{laser}} \cdot I_0 e^{-\frac{nr^n}{w^n(z)}} \quad (1)$$

with Abs_{eq} the equivalent absorptivity defined in (2), P_{laser} the laser power, I_0 the irradiated surface, n and N the coefficient values for the beam divergence.

Depending of the intensity of the interaction, the laser beam can be trapped and multi-reflected into the cavity, leading to an important increase of the absorbed energy. Moreover, by passing through the vapor media, other complex phenomena like retro-diffusion, can play a non-negligible role in the resulting laser beam distribution. These complex mechanisms are simplified in this work by using an analytic approach for the equivalent surface absorptivity as a function of the cavity geometry:

$$\text{Abs}_{\text{eq}} = \frac{\varepsilon_0[1+(1-\varepsilon_0)(\sigma-\sin^2\theta)]}{\varepsilon_0(1-\sigma)+\sigma} \quad (2)$$

with ε_0 the material emissivity, $\sigma = s/S$, s the opening surface, S the total cavity surface and θ the opening angle of the cavity.

2.2 The thermal problem

In order to evaluate the temperature evolution in the entire domain as a function of time, energy equation is solved in its classical convection/diffusion form:

$$\rho C_p \frac{\partial T}{\partial t} + \rho C_p \mathbf{u} \cdot \nabla T = \nabla \cdot (k \nabla T) + Q_i \quad (3)$$

with ρ the density, C_p the heat capacity, k the conductivity, T the temperature, \mathbf{u} the fluid velocity vector and Q_i the volume source terms.

The melting phase change is taken into account by using an enthalpy method:

$$C_p = C_p^*(T) + \delta C_p * L_f \quad (4)$$

with $C_p^*(T)$ the heat capacity as a function of temperature known from [3], L_f the melting latent heat and

$$\delta C_p = \frac{1}{\Delta T \sqrt{\pi}} e^{-\left(\frac{T-T_{\text{fusion}}}{\Delta T}\right)^2} \quad (5)$$

with ΔT the temperature range and T_{fusion} the melted point of the material.

Concerning the source term, two fluxes act at the interface: the absorbed one (1) and the evaporation one, defined by:

$$\text{Flux}_{\text{evap}} = \dot{m}(T) \cdot L_v \quad (6)$$

with L_v the vaporization latent heat and \dot{m} , the net mass flux leaving the interface equal to:

$$\dot{m} = (1 - \beta) \sqrt{\frac{M}{2\pi RT}} p_{\text{sat}}^{\text{Clapeyron}} \quad (7)$$

with β the re-condensation rate set to 0,85 [4] and the Clapeyron pressure:

$$p_{\text{sat}}^{\text{Clapeyron}} = p_0 e^{\frac{L_v M}{RT_{\text{vap}}}\left(1 - \frac{T_{\text{vap}}}{T}\right)} \quad (8)$$

with p_0 the reference pressure, R the ideal gas constant and M the molar mass.

2.3 The fluid modelling

Navier-Stokes equations are used to describe the fluid flow in the entire domain:

$$\nabla \cdot \mathbf{u} = 0 \quad (9)$$

$$\rho \frac{\partial \mathbf{u}}{\partial t} + \rho(\mathbf{u} \cdot \nabla)\mathbf{u} = \nabla \cdot [-p\bar{\mathbf{I}} + \eta(\nabla\mathbf{u} + \nabla\mathbf{u}^T)] + \rho\mathbf{g}\beta(T - T_{\text{fusion}}) + \mathbf{F}_{NS} \quad (10)$$

with ρ the density, C_p the heat capacity, k the conductivity, T the temperature, \mathbf{u} the fluid velocity vector and \mathbf{F}_{NS} the volume source terms.

The solid phase is classically assumed to behave as a liquid of very high viscosity ($\eta_{solid} = 1000$ Pa.s) when the temperature is below the melting point.

Regarding the interface condition, the recoil pressure depends on the temperature. Therefore, it leads to a strong thermo-hydraulic coupling:

$$p^{recoil} = \frac{1+\beta}{2} \cdot (p_{sat}^{Clapeyron}(T) - p_{ext}) \quad (11)$$

with p_{ext} the ambient pressure.

In order to minimize the interface deformation, capillary effects counterbalance this recoil pressure by acting in the normal direction as:

$$\mathbf{F}_{TS}^{Laplace} = \gamma(\nabla_s \cdot \mathbf{n})\mathbf{n} \quad (12)$$

with \mathbf{n} the normal vector of the interface.

Due to variations of the surface tension coefficient with temperature, $\gamma = \gamma_0 + \frac{d\gamma}{dT}(T - T_{vap})$, tangential effects (known as Marangoni effects) are also considered in this work:

$$\mathbf{F}_{TS}^{Marangoni} = \nabla_s \gamma \quad (13)$$

with ∇_s representing the surface gradient.

3. Numerical Aspects

3.1. The phase-field approach

In order to represent the behavior of the gas trapped into the welding pool, an eulerian method is used. Two kinds of fixed mesh method are available in COMSOL Multiphysics: the Level Set and the Phase Field methods. Both approaches have been tested and give the same results for low surface tension of the liquid metal (less than 0.5 N.m⁻¹). For high surface tension coefficient values, the model convergence is difficult to obtain with the Level Set method. The Phase Field approach leads then to an easier convergence of the problem.

In this case, the two-phase flow dynamics is described by the Cahn-Hilliard equation. The

method consists in tracking a diffuse interface separating the immiscible phases (region where the dimensionless phase field variable ϕ goes from -1 to 1). Due to the 4th order derivative in the Cahn-Hilliard equation, COMSOL Multiphysics solves it by means of two 2nd order equations:

$$\frac{\partial \phi}{\partial t} + \mathbf{u} \cdot \nabla \phi = \nabla \cdot \frac{\kappa \lambda}{\varepsilon^2} \nabla \psi \quad (14)$$

$$\psi = -\nabla \cdot \varepsilon^2 \nabla \phi + (\phi^2 - 1)\phi \quad (15)$$

with \mathbf{u} the velocity vector, ϕ the phase field variable, κ the mobility, λ the mixing energy density, and ε the interface thickness parameter.

The mixing energy density and the interface thickness are related to the surface tension coefficient (γ) through the following relation:

$$\gamma = \frac{2\sqrt{2} \lambda}{3 \varepsilon} \quad (16)$$

The variable χ is linked with the mobility κ and with ε by the relation $\chi = \kappa/\varepsilon^2$. The choice of the phase field parameters (ε, χ) and the mesh size (h) is essential to ensure the convergence and the accuracy of the model. Numerical validations concerning mass conservation have been performed and the same methodology as detailed in [5] has been used.

Finally, linear relations are used to link all the physical properties (ρ, η, k, C_p) to the phase field variable (ϕ).

3.2 Interfacial conditions

A major advantage of the PF formulation is its ability to treat complex interface topology. However, in order to apply surface conditions at the interface (thermal fluxes or recoil pressure defined previously), a smoothed representation of the interface between the two phases has to be used. Inspired from [6], a numerical function δ is then defined by:

$$\delta = 6V_f(1 - V_f) \frac{|\nabla \phi|}{2} \quad (17)$$

with $V_f = \frac{1+\phi}{2}$ the volume fluid fraction.

All previous surface conditions, like recoil pressure (10) for example, are “converted” to volume condition by using this δ -function:

$$\mathbf{F}_{NS} = p^{recoil} * \delta * \mathbf{n} \quad (18)$$

with the normal vector obtained from $\mathbf{n} = \frac{\nabla\phi}{|\nabla\phi|}$.

3.3 Geometry and Mesh

As only one impact is considered, an axisymmetric assumption is used. The geometry is shown Figure 2. The mesh is refined where the interface can possibly move during the whole computation.

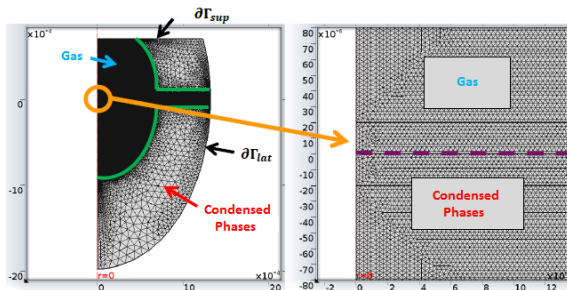


Figure 2. Geometry and mesh

All the previous equations ((3), (9), (10), (14) and (15)) are then solved in the entire domain. Concerning the solver properties, a direct approach is used to solve the linearized problem with the PARDISO solver and the BDF solver is used for the time-dependent terms. The required computational time for both the interaction and the cooling phases is roughly 10 hours with a Personal Computer of 2 processors and 32Go RAM.

4. Results

In order to validate the numerical model, confrontations with experimental data from [2] are achieved. The interaction phase is firstly studied by comparing the numerical results with different geometrical criteria and two different laser powers. The cooling stage is then detailed to understand the keyhole collapse mechanisms. At last, an example of how the model can be used to improve the process is illustrated.

4.1 The interaction phase

The laser power is set to 1000W and the properties detailed in [2] are used. A comparison

between experimental and numerical melted zones is shown Figure 3 at two different instants ($t = 5ms$ and $t = 10ms$). The results are in good agreements concerning the shapes of the melted zones. Fluid velocity vectors are also plotted with red arrows and indicate the presence of recirculation areas and strong convective flows in the melted pool when the keyhole depth increases.

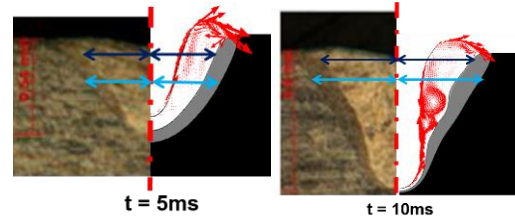


Figure 3. Experimental (left) vs numerical (right) melted zones at two different times

In order to achieve a more quantitative comparison, the numerical evolution of 4 geometrical criteria (and the corresponding experimental data) is proposed Figure 4 for two different laser powers $P_{laser} = 500W$ and $P_{laser} = 1000W$.

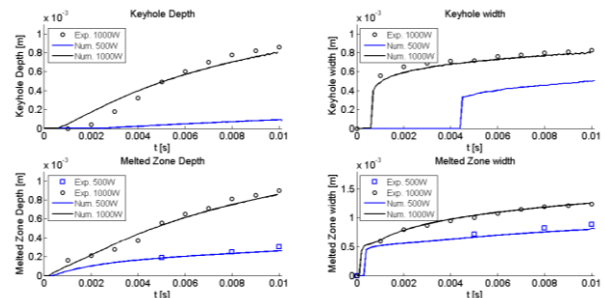


Figure 4. Comparison between experimental (markers) and numerical results (lines) for 4 criteria and 2 laser powers.

Results are in satisfying agreements for all the criteria. Indeed, the evolution as a function of time of the depths as well as the widths follow the experimental tendencies for the two laser powers. Small differences are found for the keyhole and the melted zone depths at the first times, when the keyhole is generated. It can be explained by the use of the analytical model concerning the equivalent surface absorptivity. However, these results permit to validate the assumptions used for our modeling which is now suitable to investigate other operating conditions.

To conclude this study on the interaction stage, the melted pool thickness evolution as a function of time is shown for three different laser powers (Figure 5). Three different regimes of digging can then be identified:

- The “conduction mode”, when the melted pool is thick and the resulting melted zone shape is circular,
- The “capillary mode”, when recoil pressure is stronger than surface tension effects and the melted pool thickness strongly diminishes,
- The “instable mode”, close to the capillary mode at the first times but which can lead to ejection of the liquid and strong oscillations.

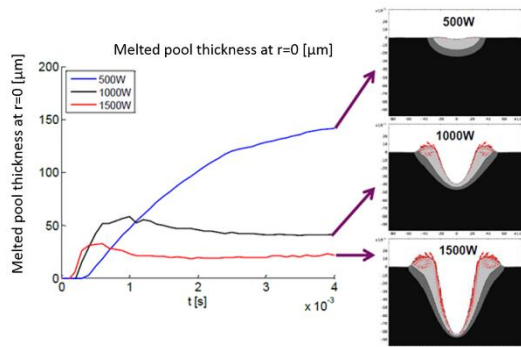


Figure 5. Melted pool thickness evolution for 3 different laser powers and resulting melted pool shapes.

4.2 The cooling phase

The cooling phase begins when the laser shoot ends. The energy deposition suddenly decreases, causing a diminution of the interface temperature and a fall of the recoil pressure. In order to ensure the mechanical (and thermodynamic) balance, surface tension forces act to close the keyhole.

With the phase field method, the interaction and the cooling phases are computed in a same model. Two different durations of laser pulse 7.8ms (Figure 6) and 11.8ms (Figure 7) are performed and resulting melted pools evolutions are shown and colored by the temperature field.

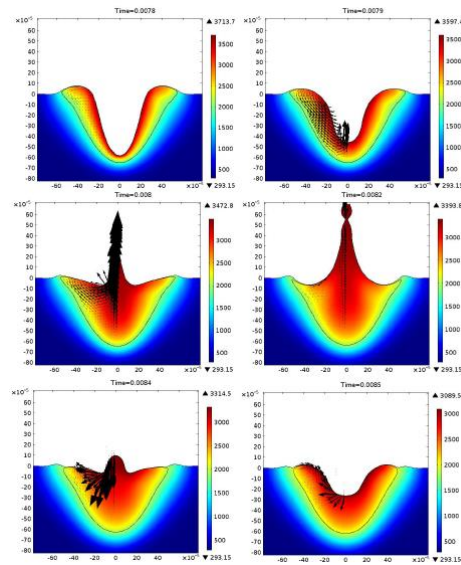


Figure 6. Keyhole collapse without bubble trapping, Temperature evolution in condensed phases [K].

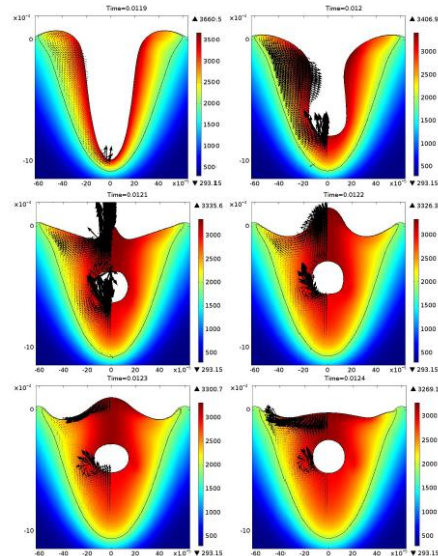


Figure 7. Keyhole collapse with bubble trapping, temperature evolution in condensed phases [K]

Two mechanisms of keyhole closure are identified, depending of the keyhole geometries as shown in [7]. In Figure 6, the geometric aspect ratio (depth over width) of the keyhole is high and a collapse from the bottom is occurring. In Figure 7, the aspect ratio is lower and the liquid-gas interface has not enough time to ascend. The keyhole collapses from the top leading to gas entrapment. The trapped bubble is then subjected to different effects like convective effects in the

melted pool, buoyancy effects and Marangoni effects. Depending of these complex combinations and obviously of the cooling kinetics, a porosity can be formed.

4.3 Welding process improvement

Based on experimental validations, the model has thus been used to describe the entire life of the keyhole from cradle to grave. As shown previously and in order to prevent the porosity formation, the keyhole closure must happen from the bottom. A way to incite this mechanism is to modify the laser pulse as a function of time in order to control the rise of the melted pool.

Two examples are shown Figure 8 by comparing the numerical results with or without pulse shaping modifications (the two different laser pulse shapes are plotted in red Figure 9). The difference in terms of closure kinetics is shown in Figure 8.

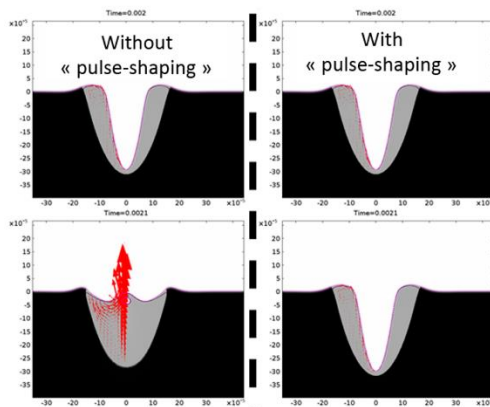


Figure 8. Keyhole closure without (left) or with (right) modification of the pulse laser shape

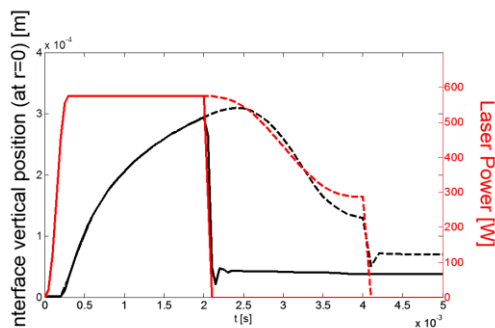


Figure 9. Comparison of two laser pulse shapes (red curves): without modification (straight line) and with modification (dotted line) – Interface vertical position at $r=0$ (black curves)

As expected, by slowly reducing the laser energy deposit on the surface, the interface rises gradually (Figure 9, in dotted black line) and the closure occurs from the bottom, reducing the probability of bubble entrapment. By using parametric analysis, this thermo-hydraulic model is now relevant to provide appropriate pulse shapes, corresponding to industrial needs.

5. Conclusions

A thermo-hydraulic model has been developed by using COMSOL Multiphysics. With the Phase Field approach, the interaction and the cooling phases have been modeled for an isolated impact. Numerical results have been compared with experimental measurements, and good agreements have been found for each criterion. Different regimes of digging and closure of the keyhole have been identified. At last, a concrete industrial application has been presented, highlighting the role of this kind of model.

6. References

1. Semak, W., Bragg, W.D., Damkroger, B., and Kempkas, S., Temporal evolution of the temperature field in the beam interaction zone during laser-material processing, *J. Phys. D: Appl. Phys.*, 32, 1819-1825 (1999)
2. Touvrety-Xhaard, C., *Etude thermohydraulique du soudage impulsif de l'alliage TA6V*. Ph.D. thesis, Université de Provence (Aix-Marseille I) (2006).
3. Robert, Y. *Simulation numérique du soudage du TA6V par laser YAG impulsif: caractérisation expérimentale et modélisation des aspects thermomécaniques associés à ce procédé*, thesis, Mines Paris (ParisTech) (2007).
4. Hirano, K., *Study on striation generation process during laser cutting of steel*, thesis, ENSAM (ParisTech) (2012).
5. Bruyere, V. Touvrety, C. and Namy, P., *Comparison between Phase Field and ALE Methods to model the Keyhole Digging during Spot Laser Welding*, Proceedings of the 2013 Comsol Conference, Rotterdam, (2013)
6. Boiling water, *COMSOL Tutorial*.
7. Bruyere, V., Touvrety, C. and Namy, P., *Thermohydraulic modeling of pulsed laser welding*, 404, International Congress on Applications of Lasers & Electro-Optics, Miami, (2013)